Fuel 347 (2023) 128502

Contents lists available at ScienceDirect

Fuel

journal homepage: www.elsevier.com/locate/fuel

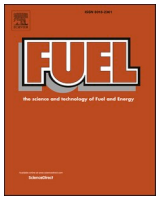

Full Length Article

IDDES simulation of hydrogen-fueled supersonic combustion based on dynamic zone flamelet model

Zheng Zhang [a], Wei Yao [a,b,*], Qiu Wang [a], Wei Zhao [a,b]

[a] State Key Laboratory of High Temperature Gas Dynamics, Institute of Mechanics, CAS, No. 15 Beisihuanxi Road, Beijing 100190, China
[b] School of Engineering Science, University of Chinese Academy of Sciences, Beijing 100049, China

ARTICLE INFO

Keywords:
Supersonic combustion
Dynamic zone flamelet model
Low-Reynolds correction
Hydrogen
Improved Delayed Detached Eddy Simulation

ABSTRACT

Based on the dynamic zone flamelet model (DZFM), the turbulent combustion of the DLR supersonic combustor with a wedge-shaped flame holder is numerically studied by IDDES. The mixing-relevant flow structures, combustion characteristics, and reaction paths were analyzed. The significant variation of flame modes, turbulence-chemistry interaction modes, and correlations between species (Y_{OH}) and mixture fraction suggests that applying a single flamelet for the whole physical space may introduce remarkable errors in describing the reacting states. Dynamically partitioning the flow field based on multiple zone division indices can effectively reduce conditional fluctuations and make the first-order closure assumption more valid. The results also demonstrate the necessity of a low-Re modification to DZFM, even for supersonic combustion.

1. Introduction

In recent decades, the scramjet has received extensive attention as one of the most promising engines for hypersonic vehicles. Due to its superiority in specific impulse, the scramjet shows excellent potential for long-range yet fast civil transport and repeatable round-trip flight for space exploration [1]. Ground testing for scramjet operating at high Mach flight conditions is challenging, and it is usually hard to achieve a long-period test. Moreover, considering the extremely high cost and the limited available measurement techniques, the flight experiments are unsuitable during the design stage of a scramjet. High-fidelity Computational Fluid Dynamics (CFD) modeling that can simulate extreme flight conditions is becoming one of the indispensable approaches in the fundamental study and concept design of scramjet engines [2-4].

However, resolving supersonic combustion is usually challenging because of the complex physics and the formidable computational cost [5]. Typically, there are strong shock waves and their complex interactions with other flow patterns, such as boundary layer [6], shear layer [7,8], and vortexes [9]. Under such complex distortions, the modes of turbulence-chemistry interaction become highly heterogeneous and evolve rapidly in the combustor [10-12]. As a result, the combustion in scramjet engines is inherently unstable and contains a broad range of characteristic time and length scales, raising significant challenges for its modeling [13-15]. High-fidelity numerical methods, such as large eddy simulation (LES) or direct numerical simulation (DNS), are necessary to accurately capture the details of the combustion process and reveal the instability mechanism and mode transition of the supersonic combustion [16-18]. However, in practical combustor design, LES simulations on grids with tens or hundreds of millions of cells undoubtedly require huge computational costs, especially for combustion models involving tens or even hundreds of elementary reactions. It is estimated that the direct integration (DI) of combustion chemistry takes>50% of the total modeling time [19]. There are two main approaches to relieving the computing load of resolving combustion chemistry. One is the direct acceleration methods, including the mechanism reduction techniques, such as DAC [20] and ISAT [21], and accelerating the direct integration of stiff reaction systems with the aid of GPU acceleration [22] or Artificial Neural Network (ANN) [23]. The alternative approach adopts the moment method based on conserved scalars, such as the variants of flamelet models [13,14] and the Conditional Moment Closure (CMC) model [15,16]. The above models reduce the dimension of the manifold of reaction systems by transforming the status of reacting scalars to a distribution function in the multi-dimensional state space coordinated by the conserved scalars, e.g., mixture fraction and reaction progress variables. Using such models, the computational cost of combustion modeling assuming detailed mechanisms with large numbers of species and stiff reactions can be reasonably and significantly reduced relative to that of the finite-rate models, such as PaSR [17] and EDC [18].

* Corresponding author at: State Key Laboratory of High Temperature Gas Dynamics, Institute of Mechanics, CAS, No. 15 Beisihuanxi Road, Beijing 100190, China.
E-mail address: weiyao@imech.ac.cn (W. Yao).

https://doi.org/10.1016/j.fuel.2023.128502
Received 2 November 2022; Received in revised form 13 April 2023; Accepted 20 April 2023
Available online 27 April 2023

Nomenclature

D_α	mass diffusivity of the species α, m^2 / s
D_T	thermal diffusivity of the species α, m^2 / s
Da	Damköhler number
e_Q	transport term representing molecular diffusion, kg/s
$\widetilde{H}_t$	total absolute enthalpy, J/kg
Ka	Karlovitz number
l_η	Kolmogorov space scale, m
$\dot{m}_{\mathrm{fuel,mxied}}$	mass flow rate of fuel participating in reactions, kg/s
$\dot{m}_{\mathrm{fuel,total}}$	total mass flow rate of fuel, kg/s
Ma	Mach number
$\overline{p}$	average pressure, Pa
Q_T	conditionally averaged temperature, K
Q_α	conditional means of species mass fractions
Q'_α	conditional fluctuation of species mass fractions
R	gas constant,J/(kg • mol)
t	time, s
$\widetilde{T}$	average temperature, K
u_i	velocity component in the i_{th} direction, m/s
x_i	Cartesian coordinate in the i_{th} direction, m
y	transverse coordinate
Y_α	mass fraction of species α

Greek symbols

δ_L	laminar flame thickness, m
ε	dissipation rate of turbulence kinetic energy, m^2 / s
η	sampling variable in the mixture fraction space
η_{mix}	mixing efficiency
λ_2	Lambda-2 vortex criterion,s^{-2}
ν	kinetic viscosity, m^2 / s
$\widetilde{\xi}$	average mixture fraction
$\widetilde{\xi''^2}$	mixture fraction variance
ξ_{react}	fuel mass fraction participating in reactions
ξ_{st}	stoichiometric mixture fraction
$\overline{\rho}$	average density, kg/m^3
ρ_η	conditionally averaged density, kg/m^3
τ_c	chemical time scale, s
$\widetilde{\tau}_{ij}$	shear-stress tensor,N/m^2
τ_t	turbulent time scale, s
τ_η	Kolmogorov time scale, s
χ	scalar dissipation rate, m^2 / s
$\Psi_{T,j}$	turbulent fluxes of enthalpy, J/(m•s)
$\Psi_{\xi,j}$	turbulent fluxes of mixture fraction, kg/(m•s)
ω	vorticity
ω_α	chemical reaction rate, kg/(m^3 • s)

Abbreviation

Baro	baroclinic torque term of vorticity transport equation
Diff	diffusion term of vorticity transport equation
Dila	dilatation term of vorticity transport equation
DZFM	dynamic zone flamelet model
TCI	turbulence-chemistry interaction
TFI	Takeno flame index
IDDES	Improved Delayed Detached Eddy Simulation
VS	vortex stretch term of vorticity transport equation

The closure of nonlinear chemical source terms with high turbulent scalar fluctuations in supersonic combustion [24] has not been given sufficient attention by the combustion modeling community. Compared with subsonic combustion, the combustion within the scramjet bears a high-Re turbulent flow, where the Kolmogorov scale of the turbulence is comparable to or smaller than the scale of reaction zones. The penetration of eddies into the flame front strengthens the coupling between turbulence and chemistry. More likely, the structures of the reaction zone within the flame are dominated by turbulent pulsation rather than by molecular diffusion, as in laminar flames [1]. Therefore, the capability of the flamelet model based on an ensemble of thin laminar flamelets for turbulent supersonic combustion is questionable. The conditional-moment-based models [25–28] adopt a similar flamelet concept, but the "flamelet" (conditional moment) is constructed based on the conditional averaged species transport equations and mapped in the conditional space. Therefore, their applications are not restricted by the thin flamelet assumption. To accurately close the chemical source term in the conditional space, it is necessary to have small fluctuations of reacting parameters, i.e., the mass fractions of species and enthalpy fluctuate mildly around their conditional means. For subsonic combustion, a first-order closure model based on a single conditional variable (single conditioning) can give good predictions of the experiments [29]. However, for supersonic combustion, where the turbulence-chemistry interaction (TCI) modes vary significantly in the domain, the single conditioning can not guarantee the first-order closure model's validation due to the weak correlations between the reacting scalars and the single conditioning variable. For this, two specific extensions to the singly-conditioning, first-order moment closure model are developed, i.e., (1) the double-conditioning model [30] to reduce the fluctuations of the reacting scalars deviating from the conditional means, especially for the non-premixed and premixed modes coexisting flame [31], and (2) the second-order closure [32] to directly diminish the error introduced in closing the conditionally averaged source terms. Although those extended models improve the accuracy in describing spatiotemporally varying TCI modes, they also increase the number of equations to be solved and complicate the closure of conditionally averaged terms, especially the higher-order moments, which still lack sufficient verification from experiments or DNS data [33]. For the LES simulations implemented with detailed reaction mechanisms, using a double-conditioning or second-order moment model will significantly increase the computational cost and complexity, which is not suitable for applications in practical combustion devices.

Following the concept of a flamelet-like model based on the conditional moment, a zonal flamelet model has been proposed recently [34]. To reduce the conditional fluctuations, a zone division strategy is used by assuming that species and temperature fluctuations within each zone can be controlled to be small around the local conditional means. The zone is divided by flow variables rather than solely by coordinates, and therefore the TCI modes of the cells contained within each zone can be controlled to be similar by properly selecting the zone division indices. The dynamical zoning method weakens the statistical dependence of the local reacting states on space other than that which are embedded in the conditioning variables and realizes a strong correlation between the single conditioning scalar (e.g., mixture fraction) and conditioned reacting scalars, i.e., an accurate representation of the local reacting state by the zonal flamelet (the local distribution of conditional moments in the conditional space with each zone). Through dynamically updating the zone division to maintain a low conditional fluctuation level within each zone, the traditional singly-conditioning, first-order moment closure model becomes applicable for highly transient and high-Re supersonic combustion [35,36].

In this study, the dynamic zone flamelet model (DZFM) is coupled with the Improved Delayed Detached Eddy Simulation (IDDES) to achieve efficient yet accurate modeling of a model scramjet of DLR [37], which has been numerical investigated using flamelet [3,38] or finite-rate [38-40] models due to its abundant experimental data [37,41].

This study aims to verify the capability of DZFM in supersonic combustion with the challenge of various flame modes ranging from diffusion to premixed and complex turbulent-chemistry interaction (TCI) and to present a modification to DZFM in the low-Re condition. The numerical results are compared with the measured data, and the mixing-relevant flow structures, flame modes, and turbulence-chemistry interaction (TCI) modes in the DLR model combustor are analyzed to validate the capability of DZFM. Finally, the necessity of a low-Re modification to DZFM even for supersonic combustion is demonstrated.

2. Physical model and numerical method

2.1. Governing equations and turbulent model

The unsteady and three-dimensional compressible reactive Navier-Stokes equations are solved. All variables ($\rho, u_i, H_t, Y_\alpha, \widetilde{\xi}$) are decomposed into resolved Favre-average quantities $\widetilde{f}$ and unresolved components f'' by a spatial filter in LES. The Favre-averaged equations for the transport of mass, momentum, energy, and species are given as follows,

$$\frac{\partial \overline{\rho}}{\partial t}+\frac{\partial \overline{\rho}\widetilde{u}_j}{\partial x_j}=0 \tag{1}$$

$$\frac{\partial \overline{\rho}\widetilde{u}_i}{\partial t}+\frac{\partial \overline{\rho}\widetilde{u}_j\widetilde{u}_i}{\partial x_j}+\frac{\partial \overline{p}}{\partial x_i}-\frac{\partial \widetilde{\tau}_{ij}}{\partial x_j}=-\frac{\partial \tau_{ij}}{\partial x_j} \tag{2}$$

$$\frac{\partial \overline{\rho}\widetilde{H}_t}{\partial t}+\frac{\partial \overline{\rho}\widetilde{u}_j\widetilde{H}_t}{\partial x_j}-\frac{\partial}{\partial x_j}\left(\overline{\rho}D_T\frac{\partial \widetilde{H}_t}{\partial x_j}+\sum_{\alpha=1}^{L}\overline{\rho}D_\alpha\frac{\partial \widetilde{Y}_\alpha}{\partial x_j}\widetilde{H}_\alpha\right)-\frac{\partial \overline{p}}{\partial t}-\frac{\partial \widetilde{u}_j\widetilde{\tau}_{ij}}{\partial x_j}=-\frac{\partial \Psi_{T,j}}{\partial x_j} \tag{3}$$

$$\frac{\partial \overline{\rho}\widetilde{\xi}}{\partial t}+\frac{\partial \overline{\rho}\widetilde{u}_j\widetilde{\xi}}{\partial x_j}-\frac{\partial}{\partial x_j}\left(\overline{\rho}D_\alpha\frac{\partial \widetilde{\xi}}{\partial x_j}\right)=-\frac{\partial \Psi_{\xi,j}}{\partial x_j} \tag{4}$$

$$\widetilde{\xi''^2}=C_{var}\Delta_{sgs}\left|\nabla\widetilde{\xi}\right|^2 \tag{5}$$

$$\widetilde{H}_t=\widetilde{H}+\frac{1}{2}\widetilde{u}_i\widetilde{u}_i \tag{6}$$

$$\overline{p}=\overline{\rho}R\widetilde{T} \tag{7}$$

here t denotes the time, x_i and u_i are the Cartesian coordinate and velocity component in the i_{th} direction, respectively , $\overline{\rho}$ is the average density and $\overline{p}$ is the average pressure, $\widetilde{H}_t$ is the total absolute enthalpy as the sum of the absolute enthalpy and the kinetic energy. $\widetilde{Y}_\alpha$ is the mass fraction of the species α, D_T is the thermal diffusivity of the mixture, and D_α is the mixture-averaged mass diffusivity of the species α. $\widetilde{\xi}$ and $\widetilde{\xi''^2}$ are the mixture fraction and its variance, a constant parameter$C_{var}=0.1$ is suggested in ref. [42] and Δ_{sgs} is the filter width for subgrid. $R=R_u/W$is the gas constant determined by the molar weight of the mixture W, the universal gas constant $R_u=8.314\,\text{J}/(\text{mol}\bullet\text{K})$.

To correctly resolve the boundary layer with an affordable mesh scale, Improved Delayed Detached Eddy Simulation (IDDES) [43] is applied, which models the wall boundary layer and the central flow regions with the one-equation Spalart-Allmaras RANS model and LES model, respectively [44]. The details of the turbulent model can be found in our previous study [35]. The chemistry of hydrogen-air combustion is solved based on the detailed mechanism developed for supersonic combustion by Jachimowski [45]. The thermodynamic and transport properties of the gas mixture are calculated using the chemical kinetics package-II [46] based on the NIST-JANAF thermochemical database [47] and a CHEMKIN-format transport database. The viscosity, specific heat, and conductivity are all assumed only depend on temperature. The mixture-averaged viscosity and thermal conductivity are calculated using the modified Wilke's law [48] and the combination averaging, respectively. Mixture-averaged mass diffusivities are calculated by Bird's formula [49], where the mass conservation is achieved by setting the nitrogen as the inert gas.

2.2. Turbulent combustion model

The dynamic zone flamelet model (DZFM) [35], which is based on spatiotemporally varying flamelets within dynamically updated zones, is adopted to decouple the interaction between the chemical reaction and turbulence locally. The transportation of conditional means of species mass fractions calculated as $Q_\alpha=\langle Y_\alpha|\eta=\xi(x,t),x\in zone\rangle$ are resolved within each zone rather than the transport of Y_α, where η is the sampling variable in the mixture fraction space. The instantaneous mass fraction is related to Q_α as, $Y_\alpha(x,t)=Q_\alpha(\eta=\xi(x,t),x\in zone,t)+Q_\alpha'(x\in zone,t)$, where the conditional fluctuation Q_α' is defined as the deviation of instantaneous value from the conditional mean. Through dynamically aggregating the CFD cells for LES flow modeling into different zones according to their similarity in terms of appropriate zone division indices, e.g., mixture fraction (ξ), mixture fraction variance (ξ''^2), reaction progress variable (c), streamwise coordinate (z), and Mach number (Ma), a homogeneous reacting state in each zone can be assumed and hence achieving a strong correlation of the fluctuation of ξ and the fluctuation of Y_α in each zone. And the strong correlation would lead to $Q_\alpha'\approx 0$, which avoids the approximate closure for terms related to Q_α' and improves the accuracy of the model consequently. It should be noted that the accuracy of DZFM relies on the choice of zone division indices, which may vary under different combustion conditions, and a general rule for zone division still needs further studies.

Substituting the $Y_\alpha(x,t)$ into the instantaneous species transport equation

$$\rho\frac{\partial Y_\alpha}{\partial t}+\rho\overrightarrow{U}\bullet\nabla Y_\alpha=\nabla\bullet(\rho D\nabla Y_\alpha)+\rho W_\alpha \tag{8}$$

it arrives,

$$\begin{aligned}\rho\frac{\partial Q_\alpha}{\partial t}+\rho\overrightarrow{U}\bullet\nabla Q_\alpha-\rho D(\nabla\xi)^2\frac{\partial^2 Q_\alpha}{\partial\eta^2}+\frac{\partial Q_\alpha}{\partial\eta}\left(\rho\frac{\partial\xi}{\partial t}+\rho\overrightarrow{U}\bullet\nabla\xi-\nabla\right.\\ \left.\bullet(\rho D\nabla\xi)\right)+\left(\rho\frac{\partial Q_\alpha'}{\partial t}+\rho\overrightarrow{U}\bullet\nabla Q_\alpha'-\nabla\bullet(\rho D\nabla Q_\alpha')\right)-\rho D\nabla\xi\\ \bullet\nabla\left(\frac{\partial Q_\alpha}{\partial\eta}\right)-\rho D\nabla^2 Q_\alpha\\ =\rho W_\alpha\end{aligned} \tag{9}$$

and combining with the conservation law of ξ,

$$\rho\frac{\partial\xi}{\partial t}+\rho\overrightarrow{U}\bullet\nabla\xi=\nabla\bullet(\rho D\nabla\xi) \tag{10}$$

then taking the conditional average on condition that 1) $\xi(x,t)=\eta$ and 2) within the zone $x\in zone$, the transport equation of Q_α can be derived as [34],

$$\begin{aligned}\rho_\eta\frac{\partial Q_\alpha}{\partial t}+\langle\rho u_j|\eta\rangle_{zone}\frac{\partial Q_\alpha}{\partial x_j}+E_{ZFM}=&\rho_\eta\frac{D_\alpha}{D_\xi}\langle\chi|\eta\rangle_{zone}\frac{\partial^2 Q_\alpha}{\partial\eta^2}+\rho_\eta\left(\frac{D_\alpha}{D_\xi}-1\right)M_\eta\frac{\partial Q_\alpha}{\partial\eta}\\ &+\rho_\eta\langle\omega_\alpha|\eta\rangle\end{aligned} \tag{11}$$

where $\chi=(D_\xi+\frac{\nu_{sgs}}{\text{Sc}_t})\bullet(\nabla\xi)^2$ is the scalar dissipation, $\langle\bullet|\eta\rangle_{zone}$ indicates a quantity conditioned on the mixture fraction within a zone, $\rho_\eta=\langle\rho|\eta\rangle$ is the conditionally averaged density, $M_\eta=\langle\nabla\bullet(\rho D_\xi\nabla\xi)|\eta\rangle_{zone}$ is the conditional diffusion. The zone conditional mean of scalar dissipation rate, $\langle\chi|\eta\rangle_{zone}$ is closed using the Amplitude Mapping Closure (AMC) model [50]. The abbreviation $E_{ZFM}=e_y(Q_\alpha')+e_q(Q_\alpha)$ represents the terms related to the conditional fluctuation Q_α' and the macro-transport of Q_α

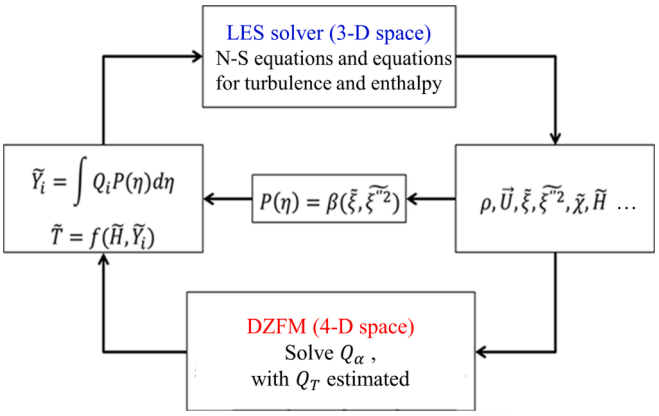

Fig. 1. The flowchart of the solving process of flow and combustion [54].

by molecular diffusion. The first term can be neglected as $Q'_\alpha \approx 0$ under a proper zone division scheme. And the second term,

$$e_Q = \langle \rho D_\alpha \nabla \xi \bullet \nabla (\partial Q_\alpha / \partial \eta) | \eta \rangle_{zone} + \langle \nabla \bullet (\rho D_\alpha \nabla Q_\alpha) | \eta \rangle_{zone} \quad (12)$$

is small for high-Re turbulent flow, where $\rho D_i \sim Re^{-1}$ following the approximate analysis in [51], and is ignored in modeling supersonic combustion with DZFM [34,36] and commonly neglected in the studies using CMC [29,32,52]. This approximation is also adopted in this paper except in section 3.4, where the DZFM model is developed to consider the molecular diffusion effect under low-Re regions.

Similar to the coarser grid used for conditional mean variables of the generic CMC model, the transport equation of Q_α (Eq. (11)) is discretized and solved in dynamically divided zones defined by the ensemble of CFD cells and η space. The Operator Splitting method is applied to solve Eq. (11). A finite volume method is used to solve the convective part in the divided zones considering the irregular geometric shape and the random number of CFD cells within each flamelet zones. The micro-mixing and differential diffusion of Q_α in the η space is solved by the finite difference method. The conditional FDF-weighted averaging method developed for high-resolution LES data [52,53] is used to estimate e_Q. And finally, the conditionally averaged chemical reaction term $\langle \omega_\alpha | \eta \rangle$ is closed by the first order approximation [51],

$$\langle \omega_\alpha | \eta \rangle = \omega_\alpha (Q_\alpha, Q_T) \quad (13)$$

with the assumption of small local conditional fluctuations. The conditionally averaged temperature Q_T is estimated with a historical statistics approach [36,52] rather than solving a conditional enthalpy equation with a series of unclosed conditional sub-models, therefore saving the computational cost. The flowchart of the solving process of flow and combustion is illustrated as shown in Fig. 1. At each time step, the cell-based data obtained by the flow solver are averaged over each zone and passed to the DZFM solver which solves equations of the conditional mean species and estimates conditionally mean temperature. The unconditional values of species mass fraction $\tilde{Y}_\alpha$, can be obtained from the integration of conditional species mass fraction stored in the local flamelet weighted by the β-function Probability Density Function (PDF),

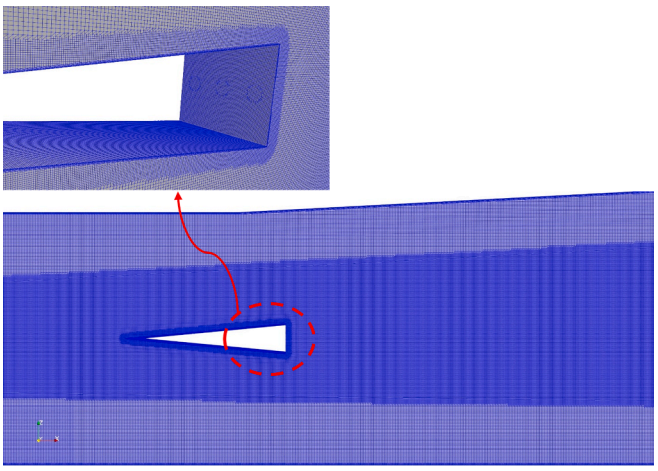

Fig. 3. Grid system of the computational domain.

$P(\eta) = \beta(\tilde{\xi}, \widetilde{\xi''^2})$ which is a function of mixture fraction $\tilde{\xi}$ and its variance $\widetilde{\xi''^2}$.

2.3. OpenFOAM-Based solver

The governing equations are solved using an OpenFOAM [55] based compressible reacting flow solver Amber, which has been validated in modeling supersonic combustion [34,36,56]. The convective fluxes at the surfaces are constructed by a second-order low-Mach-corrected hybrid KNP/central scheme [57], which can accurately resolve turbulence away from shocks while maintaining stability near the discontinuity. Total variation diminishing (TVD) limiter vanLeer [58] is used to interpolate the interface values. The temporal integration is realized by the second-order Crank-Nicholson scheme.

2.4. Test case and computational setups

The numerical setup of the DLR combustor and experimental configurations are shown in Fig. 2. The air enters the combustor at Ma = 2 through the entrance with a height of 50 mm and a width of 40 mm. The upper wall is divergent with a 3° angle after a distance of 60 mm behind the entrance. A wedge-shaped 32-mm-long and 6-mm-height strut was placed 35 mm downstream of the entrance as the flame stabilizer, where H_2 is injected through a row of 15 holes on the base. The H_2 orifices with the same diameter of 1.0 mm are equally distributed in the z-direction with a distance of 2.4 mm. The air is preheated with a H_2-air burner, accelerated through a Laval nozzle and then enters the combustor at the static temperature T = 340K and pressure p = 0.1MPa. The composition of the vitiated air is $Y_{O2} = 0.232$, $Y_{H2O} = 0.032$, and $Y_{N2} = 0.736$. H_2 is injected sonically with a temperature of 250 K and a pressure of 0.1 MPa. The reader can refer to [37] for more details of the experiment.

The numerical modeling is configured following the experiment. To alleviate the computational cost, one-fifth of the scramjet with only three injectors of the total fifteen in the experiment was included in the

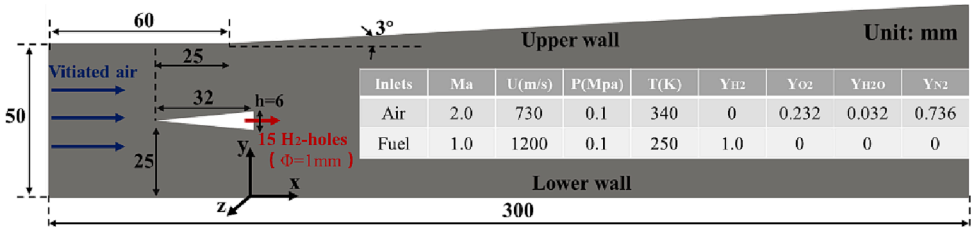

Fig. 2. Numerical setup and schematic of the DLR combustor.

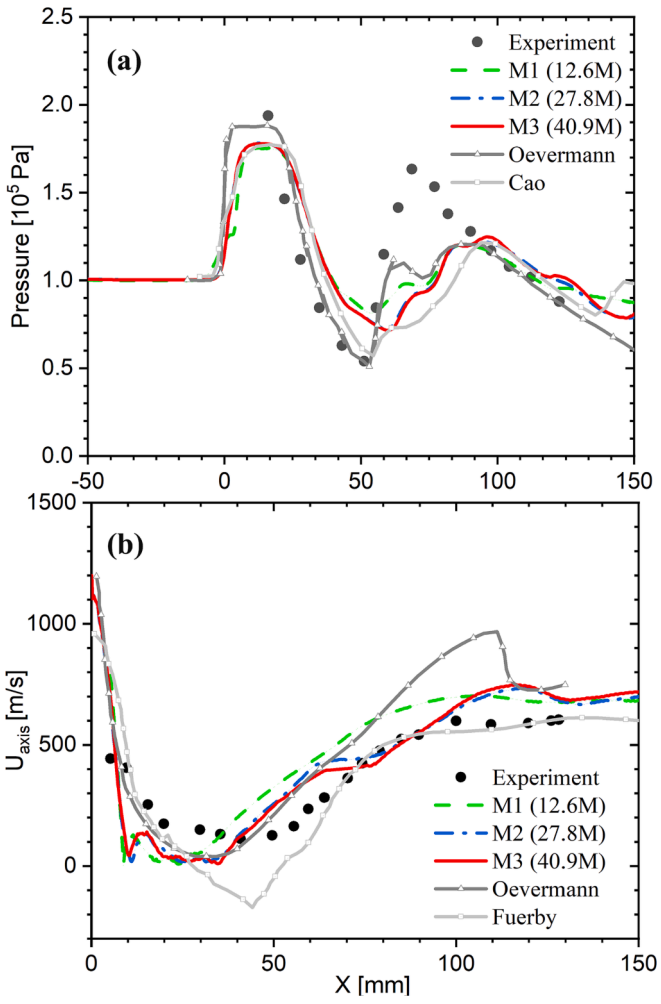

Fig. 4. Grid independence study based on (a) lower wall pressure under the frozen-chemistry condition and (b) centerline velocity for reacting flow.

computational domain, whose spanwise direction is treated by the periodic boundary condition. The grid system dominated by high-quality hexahedral cells is generated with the Cartesian cut-cell method [59]. The transition zone near the central wedge is partially filled with tetrahedron or pyramid cells, as shown in Fig. 3. A local refinement is used near the wedge and central zone with a minimum cell size of 0.05 mm and 0.15 mm, respectively. The boundary layer grid is filled with 15 exponential expansion layers, which grow from a 5-μm initial prism layer to satisfy the non-dimensional wall distance of $y^+ \sim O(1)$. The grid convergence was verified with three meshes containing 12.6 million (M1), 27.8 million (M2), and 40.9 million (M3) cells. The lower wall pressure under the frozen-chemistry condition and the center velocity for reacting flow are shown in Fig. 4. The results show that the medium and finest mesh give similar results with the relative discrepancy of 0.95% and 6.75% for the wall pressure and center velocity, respectively. Overall, the results obtained with medium and fine mesh are closer to the experiment data [41] and comparable to the numerical results from Oevermann et al. [3], Cao et al. [60], and Fuerby et al. [38]. In consideration of the computational cost, the medium-size mesh is used for the modelings if not otherwise specified. The simulation ran on Tianjin (TH-HPC4) cluster using 360 processors with a base frequency of 2.6 GHZ. The time step varied under the limitations of a maximum Courant number of 0.5 and a maximum time step of 5×10^{-8} s. The flow-through time (FTT) is 0.41 ms, which is estimated based on the length of the combustor (0.3 m) and the flow speed of the vitiated air (730 m/s). The modeling using the finest mesh takes about 91,000 CPU hours to ensure 5 FTTs for sampling and data statistics.

3. Results and discussions

3.1. Model validation

Fig. 5(a) shows the comparison between the experimental [37] and numerical ($|\nabla\rho|$) schlieren under the frozen-chemistry condition. The modeling results well reproduced the complex wave structure observed in the experiment, including the two oblique shock waves formed due to compression by the central wedge and the subsequent wave system due to transmission through the central jet and reflection between the upper and lower walls. The expansion and compression waves formed at the tail of the wedge were also well reproduced. In addition, shear layers are formed between the high-speed hydrogen flow ejected from the central orifice and the low-speed wake flow of the wedge and evolve into a series of vortex structures due to K-H (Kelvin-Helmholtz) instability. Furthermore, the current modeling well captured the interaction between reflected oblique shocks and the central sheer layers, which distorts the K-H vortex into larger structures, as observed in the experiment. There are another two incident shocks in the experiment,

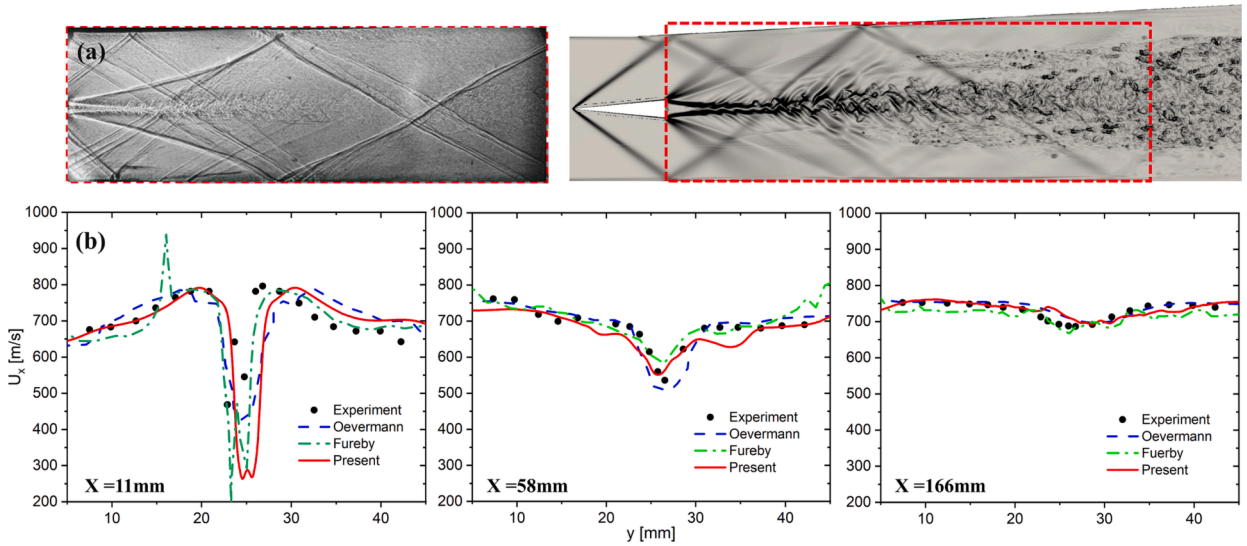

Fig. 5. Comparisons of (a) schlieren and (b) velocity profiles between numerical and experimental results under frozen chemistry.

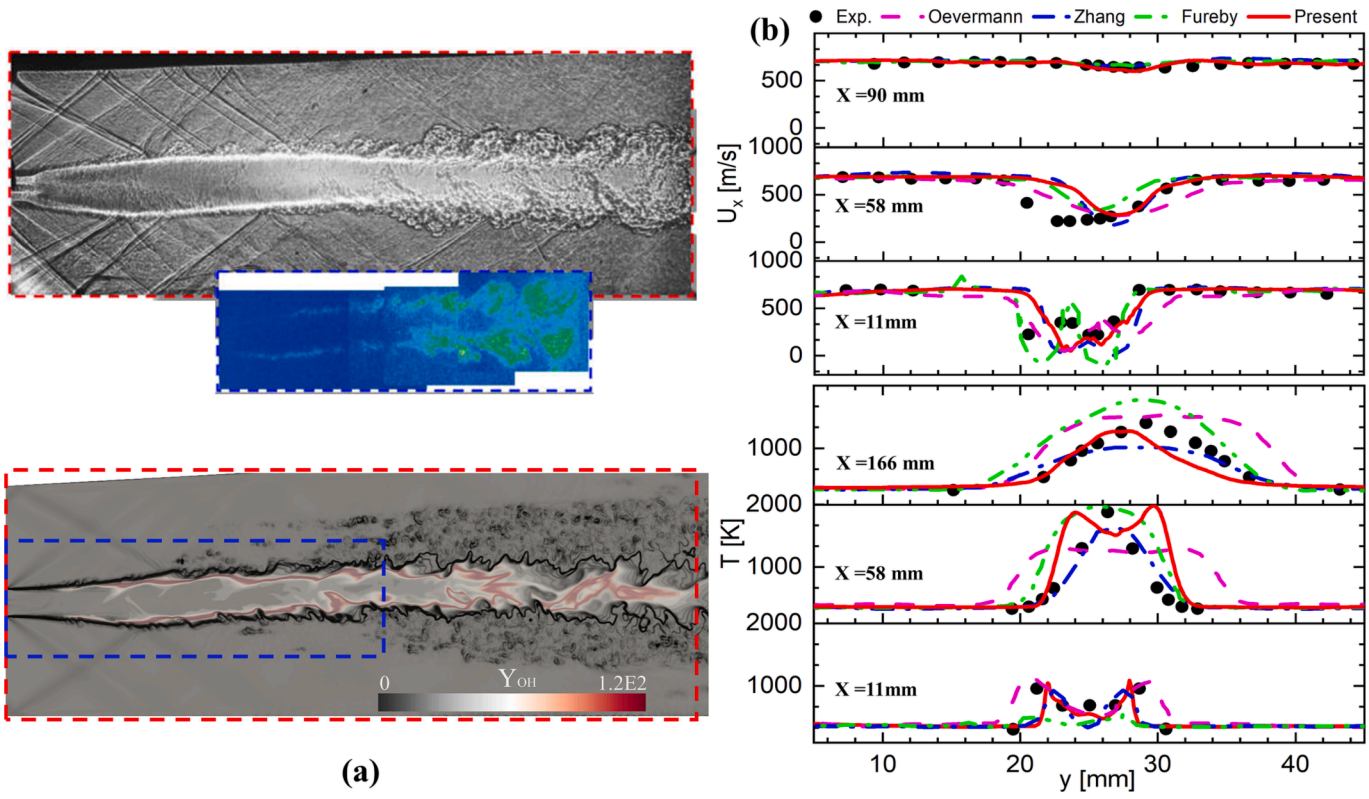

Fig. 6. Comparisons of (a) schlieren contoured by OH distribution and (b) profiles of velocity and temperature at various locations under combustion.

except the reflected shocks form the tip of the wedge, which leads to more complex wave structures through reflecting with walls and interaction between shock waves. The non-uniform inflow induced by the attached nozzle should be blamed for the difference in the incident shocks, as suggested by the comparative study of different boundary conditions from Potturi and Edwards [61].

The distributions of average velocity at different streamwise locations are qualitatively compared in Fig. 5 (b). The modeling results reasonably agree with the experimental data, especially in the downstream region. Near the hydrogen jet and the wake interaction zone (x = 11 mm), the mean velocity drops significantly at the center as the sonic hydrogen injection is mixed with low-velocity recirculation flow formed behind the wedge. The lower-velocity region owing to the larger recirculation bubble is predicted in the current modeling and in the modeling by Oevermann et al. [3] and Fureby et al. [38] and some other numerical studies [62,63]. The discrepancy may be introduced by simplifying hydrogen injectors from 15 to 3 with periodic boundary conditions in the spanwise direction, which alters the flow in the wake of the wedge [64].

Fig. 6 (a) compares the flow structure presented by the experimental and numerical schlieren for the reacting case and the flame structure contoured by the OH distribution between the OH-PLIF and numerical result. The main features of the flow structure in the experiment are well captured. The thermal expansion due to the combustion heat release affects the flow field downstream of the wedge. The recirculation flow and shear layers developed from the wedge tail are enhanced compared to the nonreacting case. With the growth of the shear layer, the expansion fan induced at the corner of the wedge weakens gradually, and consequently, the oblique shock wave formed by the convergence of shear layers disappears. In addition, the oblique shock wave reflected by walls is further reflected after contacting shear layers in the central region, while the wave is transmitted and further reflected from the up and bottom wall in the frozen-chemistry case. From the OH distribution, the lift-off phenomenon of the flame anchored by the wedge is predicted by the current modeling based on the zone flamelet concept. Compared to the experiment, OH is distributed in a slightly narrower yet longer space. The disturbance of reflected shock waves on the flame and shear layers observed in the experimental schlieren should be the principal reason for the discrepancy. Moreover the neglect of molecular diffusion terms can also be blamed, as discussed in section 3.4.

Comparisons between the calculated profiles of mean velocity and temperature and the measured data at three downstream locations are shown in Fig. 6 (b). It can be found that present simulations have a reasonable agreement with the experimental data and are similar to other numerical results [3,38,39]. Near the hydrogen jet, both modelings well predicted a wide “W” type velocity distribution due to the expansion of the recirculation zone. At the second location, the low-velocity region in the center is narrow compared with the measured data, which was also found in the other presented simulations. At the locations far from the injection (x = 90 mm), the flat velocity distribution due to turbulent mixing is well captured by all the modelings. For the mean temperature, the predictions near the tail of the wedge (x = 11 mm) of the current and other studies match well with the measurement, except the result given by [38] slightly overpredicted the lift-off distance of the flame. In the middle of the combustion chamber (x = 58 mm), the predicted mean temperature profile shows a double-peak structure consistent with the thin split flame sheets in Fig. 5 (a). The flame sheets have been merged near the combustor exit (x = 166 mm), resulting in a single peak temperature profile as observed experimentally. The comparison shows that the modeling by Oevermann [3] with the RANS method predicted a much more distributed flame structure than other LES simulations by Zhang et al.[39] and Fureby. Moreover, the agreements of all the presented LES results are overall good. Considering the difference in sub-grid model, turbulent combustion models, and combustion chemistry adopted in these LES studies, such a variety of predictions can be expected.

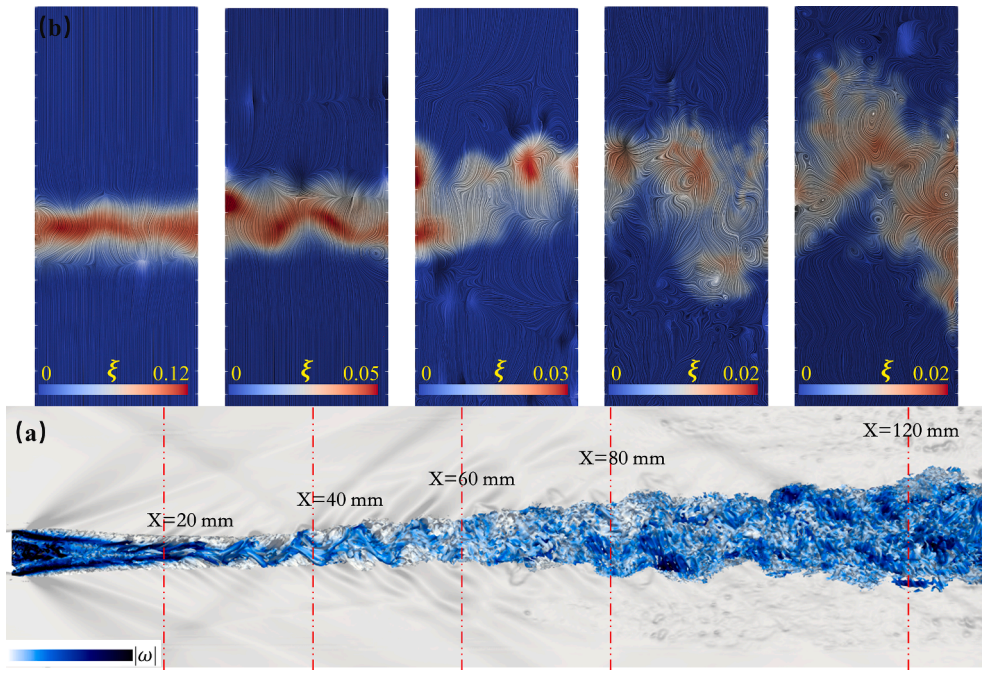

Fig. 7. (a) The vortex structure manifested by the isosurface of $\lambda_2 = -1e^8\ s^{-2}$ overlapped on numerical schlieren and colored by vorticity magnitude, and (b) contours of mixture fraction (ξ) with streamlines on x-slices at different locations for cold flow.

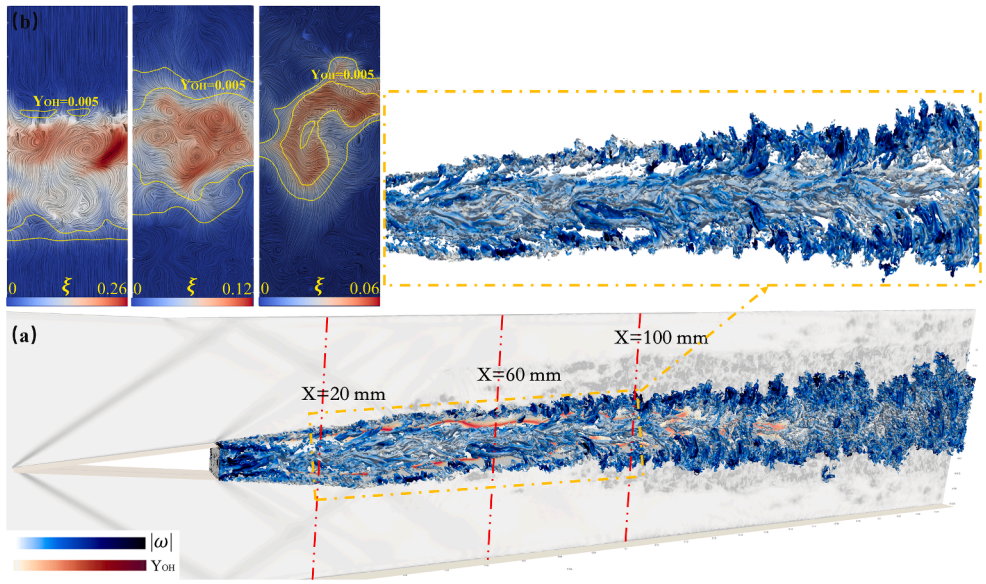

Fig. 8. (a) Isosurface of $\lambda_2 = -1e^8\ s^{-2}$ colored by vorticity and numerical schlieren overlaid by YOH contour, (b) contours of mixture fraction overlaid by streamlines on the x-slices (solid yellow lines denote YOH = 0.005). (For interpretation of the references to colour in this figure legend, the reader is referred to the web version of this article.)

3.2. Flow and mixing analysis

Fig. 7 shows the vortex structure and mixture fraction (ξ) distribution in the wake region of the wedge under frozen chemistry. From Fig. 7 (a), the two shear layers developed from the base of the wedge are rolled up due to K-H instability and interact with the asymmetric oblique shock train to form large-scale vortexes, which then shred in the form of small-scale disordered vortexes under the second instability. The above flow instability process controls the mixing between the hydrogen-enriched wake flow and the ambient air. As shown in Fig. 7 (b), the mixing of hydrogen and air is mainly controlled by the entrainment of large-scale spanwise vortices near the wedge (x = 20 ~ 40 mm), where the mixture fraction decreases rapidly, but most of the region is still under a fuel-rich condition. The shedding from downstream (x > 60 mm) strengthens the streamwise vortexes and enhances the small-scale mixing, as indicated by the much more homogeneous spatial distribution of mixture fraction.

Fig. 8 shows the evolution of vortex structure and mixture fraction in the wake region for the combustion case. For the combustion case, the mixing is affected by not only the shear instability but also the heat imposition. The volumetric expansion due to heat release causes wider shear layers and a larger wake region but also constrains the development of quasi-two-dimensional large-scale spanwise vortices. The baroclinic effect between the reacting shear layer induces randomly oriented small vortexes in the jet wake region behind the wedge.

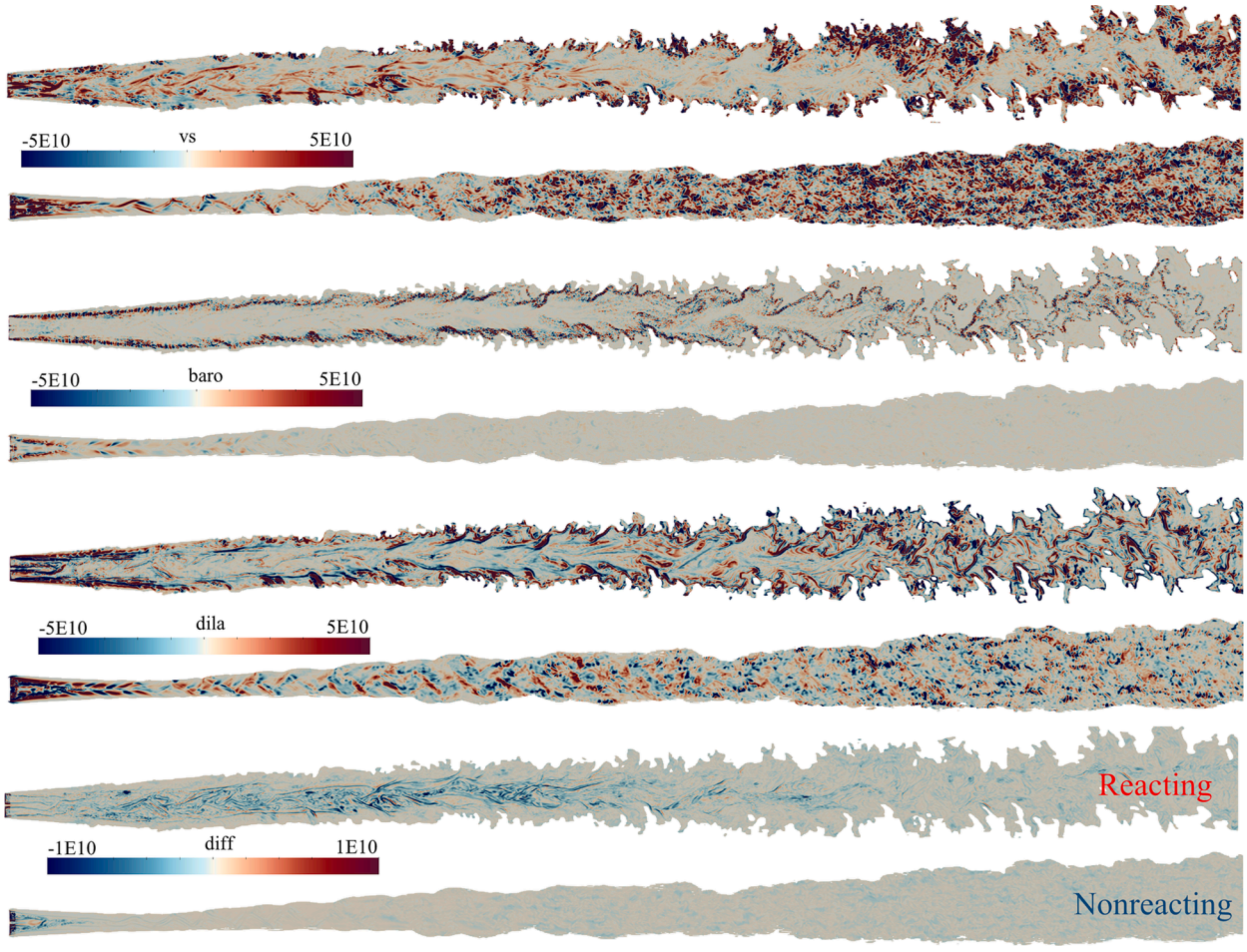

Fig. 9. Contours of transport index (vs, baro, dila, diff) of vorticity for combustion and frozen-chemistry cases.

Two small-scale vortex streets adjacent to the central vortexes are formed along the shear layers from the boundary layer separation point on the inclined surface of the wedge. The vorticity magnitude of two vortex streets increases as transferred downstream, leading to a more intense interaction with the flame. Such interaction rolls up and merges the flame sheet, which finally transforms into a pulsating and intermittent pattern. From Fig. 8 (b), the mixture fraction at the corresponding location is higher than that in the frozen-chemistry case. The hydrogen-rich wake flow is stirred by relatively small vortexes inside the flame sheets denoted by $Y_{OH} = 0.05$, leading to a more homogeneous mixture downstream.

A further analysis to identify the mechanisms of mixing can be conducted by looking at the compressible vorticity transport equation:

$$\frac{D\omega}{Dt} = \underbrace{(\omega\cdot\nabla)}_{vs} \underbrace{-\omega(\nabla\cdot u)}_{vs} \underbrace{+(\nabla\rho\times\nabla\rho)/\rho^2}_{Baro} + \underbrace{\nu\nabla^2\omega}_{Diff} \tag{14}$$

The terms on the right-hand side represent the four main physical mechanisms that contributed to the vorticity evolution through vortex stretch **VS**, dilatation **Dila**, baroclinic torque **Baro**, and diffusion **Diff**, respectively. To have an insight on the effects of different terms on vorticity evolution, the transport index obtained through the inner product between the original transport term and the unit vector along vorticity (eg. dila $= (\boldsymbol{\omega}/\|\boldsymbol{\omega}\|) \bullet \boldsymbol{Dila}$) are shown in Fig. 9. In both the reacting and chemistry-frozen cases, the vortex stretch and dilatation play an important role of vorticity transport and evolution of vortices. In the reacting case, the heat release leads to volume expansion of the upstream region near the strut, which weakens the positive effect of vortex stretch and strengthens the negative effect of dilatation on vorticity and depresses the large-scale spanwise vortex behind the strut as that in the non-reacting case. Meanwhile, the vorticity magnitude of two vortex streets along the flame surface increases because of the amplification of baroclinic torque due to misalignment between the density gradient and the pressure gradient across the flame, as shown in

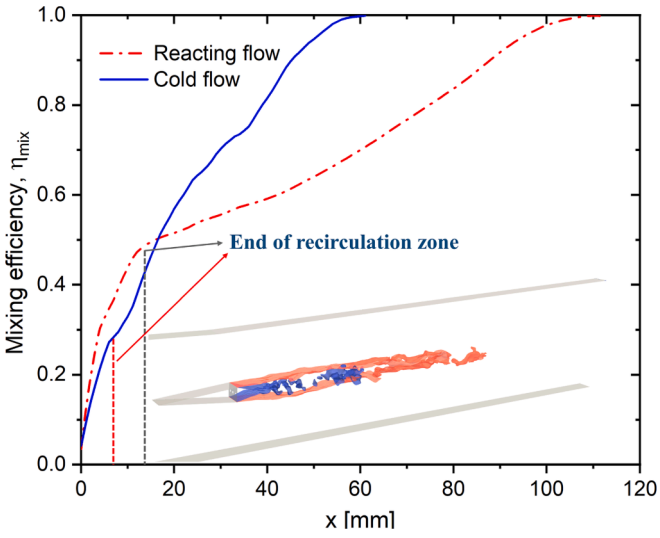

Fig. 10. Streamwise variation of mixing efficiency and contours of $\xi_{st} = 0.028$ (inset) for the frozen-chemistry and combustion cases.

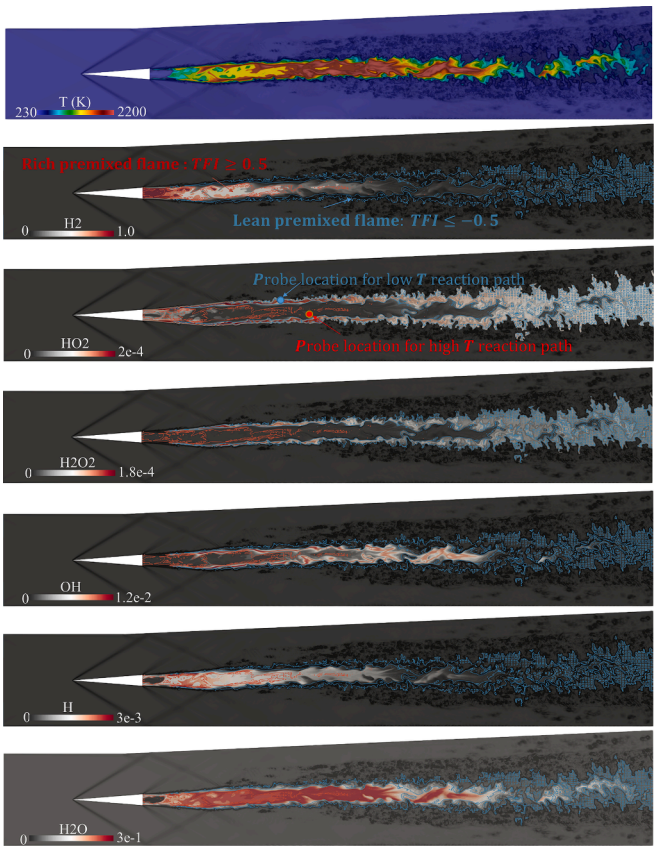

Fig. 11. Contours of instantaneous flame temperature and species on the central z-slice overlaid with the TFI contour line of ± 0.5.

Fig. 8. The diffusion term diff represents the effect of viscosity is much lower than others, which reduces vorticity through diffusion and dissipation, especially in the reacting case.

To quantitatively analyze the effect of heat release on the mixing, the streamwise variation of mixing efficiency (η_{mix}) in the frozen-chemistry and combustion cases are compared in Fig. 10. The mixing efficiency averaged over n sampling time steps is calculated as [65],

$$\eta_{mix} = \frac{1}{n}\sum_{n}\frac{\dot{m}_{\text{fuel,mxied}}}{\dot{m}_{\text{fuel, total}}} = \frac{1}{n}\sum_{n}\frac{\int(\rho \boldsymbol{u}\xi_{\text{react}})\bullet dA}{\int(\rho \boldsymbol{u}\xi)\bullet dA} \tag{15}$$

where Y_{H2} is the hydrogen mass fraction, and ξ_{react} is defined as the mass fraction of the least available reactant (fuel or oxygen depending on the global equivalence ratio) that would react if a complete reaction took place without further mixing.. When the local mixture fraction is lower than the stoichiometric mixture fraction ξ_{st}, it is considered that $\xi_{\text{react}} = \xi$, otherwise $\xi_{\text{react}} = \xi_{st}(1-\xi)/(1-\xi_{st})$. From Fig. 10, η_{mix} increases rapidly near the end of the wedge, where hydrogen is quickly mixed with the surrounding air with the aid of the strong shear flow and the recirculation zone. The larger recirculation zone in the combustion case causes better near-field mixing, where the mixing efficiency increases faster than that in the frozen-chemistry case. After the recirculation zone, the entrainment of air by the large-scale spanwise vortexes makes the mixing efficiency in the frozen-chemistry case supersede that in the combustion case, while the underdevelopment of large-scale vortexes inhibits the rise of mixing efficiency in the combustion case. It can be considered that the convective transport of the large-scale spanwise vortexes disperses the fuel rapidly and therefore dominates the mixing efficiency, while the turbulent diffusion enhanced by the small-scale vortexes is vital for homogenous mixing between fuel and oxygen indicated by a homogeneous and low distribution of mixture fraction in the downstream region as shown in Fig. 7 and Fig. 8. The baroclinic torque and thermal expansion due to heat release in reacting flow induce more diffusive small vortexes but suppress the formation of large-scale vortexes in the plume [66], resulting in a longer mixing distance for the combustion case. The inset in Fig. 10 illustrates the tortuous and broken contours of $\xi_{st} = 0.028$ due to large-scale vortex which enhancing the mixing process, especially for the frozen flow.

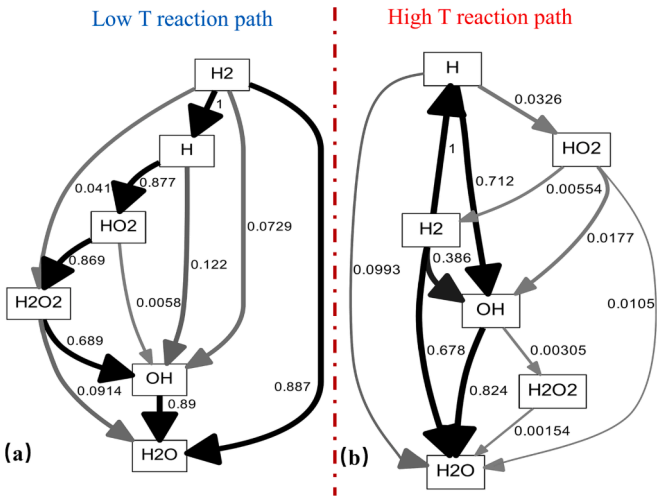

Fig. 12. Reaction path diagram of hydrogen-air premixed flame (a) at low temperature and (b) at high temperature.

3.3. Premixed flame mode and TCI mode

Fig. 11 shows the contours of flame temperature and species on the central z-slice and the distribution of flame mode based on improved TFI (Takeno flame index) [67]. In addition to distinguishing the premixing and diffusion modes by the diffusion direction (concentration gradient) between oxygen and fuel, the improved TFI also defines the rich and lean region according to the stoichiometric mixture fraction as,

$$\text{TFI} = \begin{cases} \left(\dfrac{\xi-\xi_{st}}{|\xi-\xi_{st}|}\right)\bullet\dfrac{1}{2}\left(1+\dfrac{\nabla Y_{H2}\bullet\nabla Y_{O2}}{|\nabla Y_{H2}\bullet\nabla Y_{O2}|}\right)(\xi\neq\xi_{st}) \\ \dfrac{1}{2}\left(1+\dfrac{\nabla Y_{H2}\bullet\nabla Y_{O2}}{|\nabla Y_{H2}\bullet\nabla Y_{O2}|}\right)(\xi=\xi_{st}) \end{cases} \tag{16}$$

According to Eq. (16), the flame with TFI>0.5 is in a rich premixed mode, and the one with TFI lower than −0.5 is in a lean premixed mode, otherwise in a diffusion mode. From Fig. 11, the central hydrogen jet and the shear layer have a relatively low temperature and are in the rich and lean premixed modes, respectively. The rich premixed flame is formed by intensive near-field mixing by the recirculation zone, as illustrated in Fig. 10. The small-scale vortex street produces the lean premixed flame along the shear layers. The reaction paths sampled at several representative points are shown in Fig. 12. The heat release in the low-temperature premixed flame region is mainly contributed by low-activation-energy reactions $H_2 + O_2 => HO_2 + H$ and $H + O_2 + M => HO_2 + M$. With the massive generation of HO_2, H_2O_2 is generated via $2HO_2 => H_2O_2 + O_2$·H_2O_2 and HO_2 further generate OH and H through chain branch reactions. The radicals OH and H generated in the low-temperature premixed flame region were transported into the high-temperature diffusion flame region to induce a thermal explosion of self-accelerating reactions. In the high-temperature reaction region between the low-temperature premixed regions, the reaction is dominated by chain branching reactions $H_2 + OH => H_2O + H$ and $O + H_2 => H + OH$, which consumes hydrogen and generates rich active radicals and H_2O in the central diffusion flame region. Near the domain exit, local flame quenching due to weak reactions renders an intermittent flame pattern, as shown in Fig. 11.

Fig. 13 (a) shows the distribution of the active intermediate OH

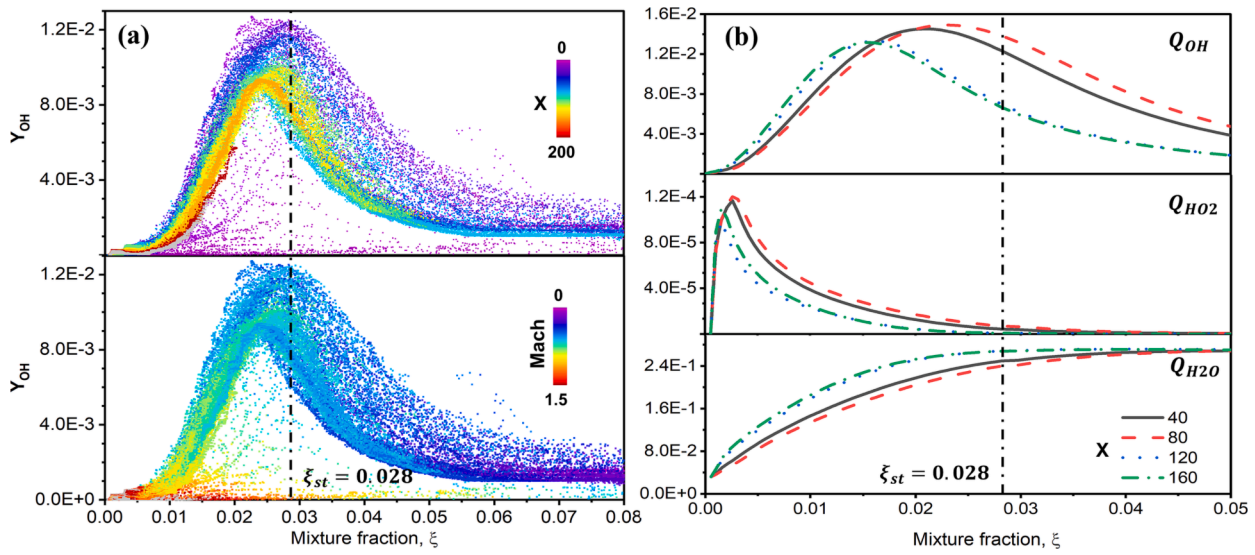

Fig. 13. (a)Y_{OH} distributed in the mixture fraction space colored by x-coordinates and Mach number and (b) profiles of the conditional means of reactive scalars in different zones.

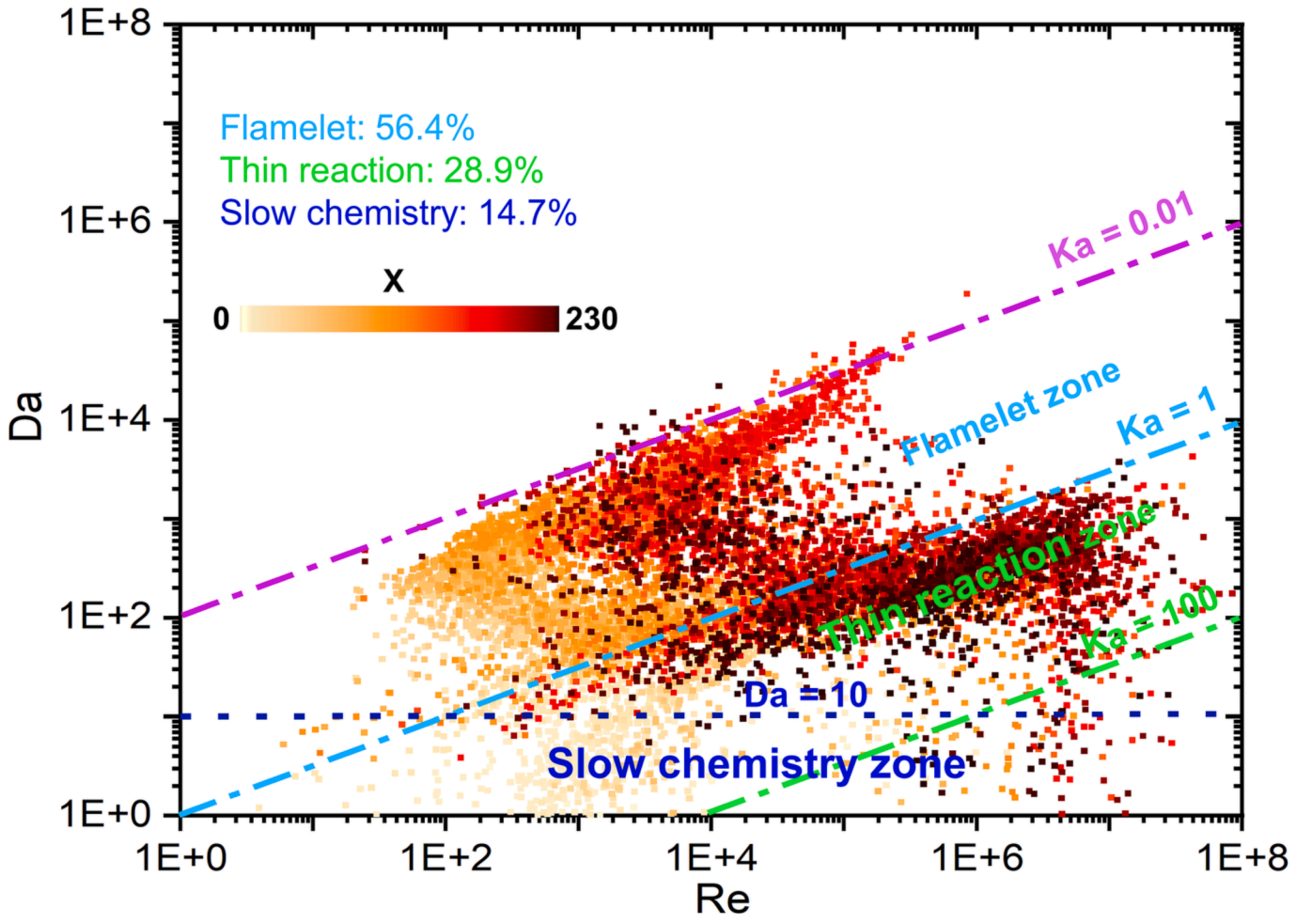

Fig. 14. Borghi diagram of TCI modes colored by × coordinates.

radical in the mixture fraction space. The significant difference in the Y_{OH}-ξ probed at different locations suggests that applying a single flamelet for the whole physical space may introduce remarkable errors in describing the reacting states in a supersonic flame. After grouping the sampling states in terms of the streamwise coordinate and Mach number, the scattering of Y_{OH} distribution within each group was significantly reduced. The strong correlations between the local reacting states denoted by Y_{OH} and mixture fraction within each subgroup

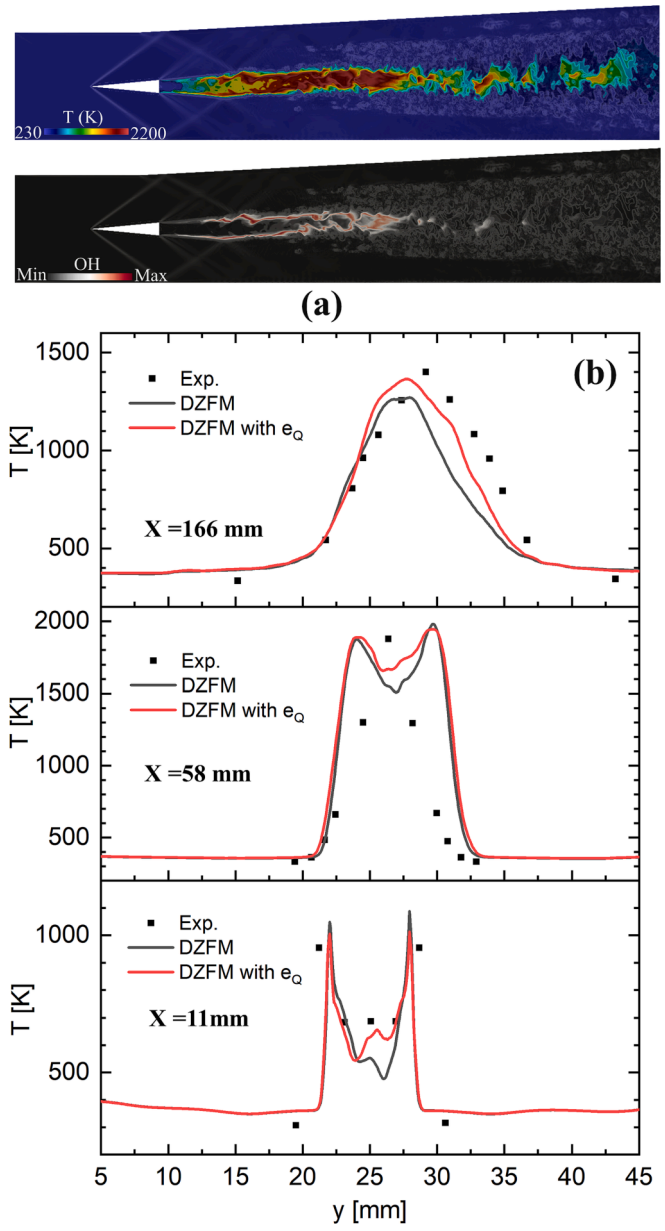

Fig. 15. Results of (a) instantaneous flame structure and (b) mean flame temperature with..e_Q

validate the physical correctness of zone-based flamelet. Fig. 13 (b) shows the evolution of the conditional profiles of reactive scalars in different zones divided by x-coordinates, which indicates the variation of flame and TCI models in the physical space, as discussed above. Therefore, dynamically partitioning the flow field based on multiple zone division indices can capture the distribution of different reaction states of the flame, effectively reduce conditional fluctuations, and make the first-order closure assumption more valid.

Fig. 14 quantitatively measures the turbulence-chemistry interaction modes by the Borghi diagram [68]. Damköhler number defined as $\mathrm{Da} = \tau_t/\tau_c$ represents the ratio of the turbulent time scale $\tau_t = k/\varepsilon$ to the chemical time scale τ_c, which is determined as the reciprocal of CEMA (Chemical explosive mode analysis) index [69,70]. Karlovitz number is defined as $\tau_c/\tau_\eta = {\delta_L}^2/{l_\eta}^2$ to weigh the chemical time scale to the Kolmogorov time scale $\tau_\eta = (\nu/\varepsilon)^{1/2}$, and scale the laminar flame thickness δ_L to the Kolmogorov space scale l_η. The Reynolds number *Re* are related to Da and Ka by $Re\,(\tau_t/\tau_\eta)^2 = \mathrm{Da}^2 \bullet \mathrm{Ka}^2$. The above dimensionless

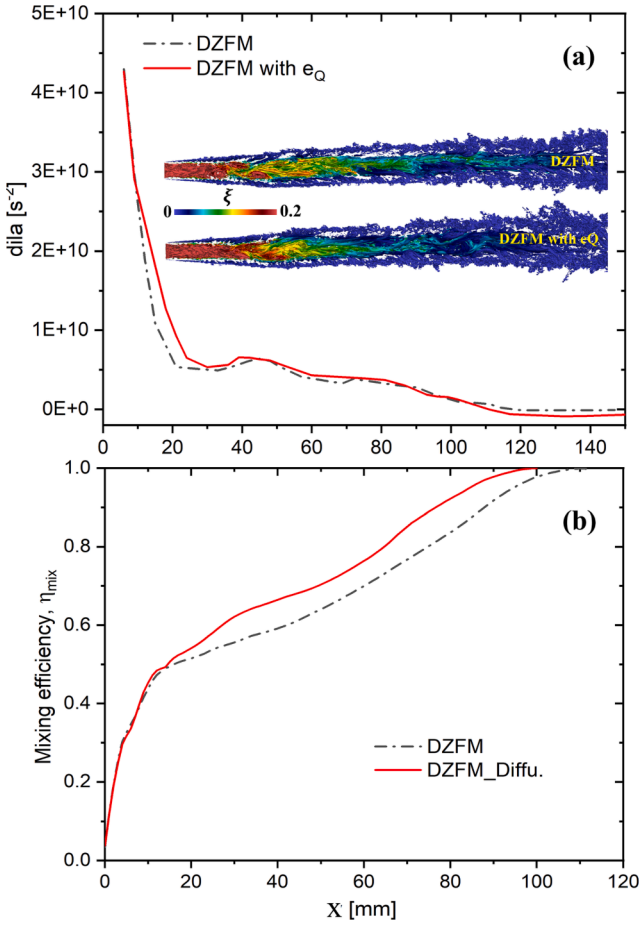

Fig. 16. Comparisons of (a) time averaged mass-flux-weighted spatial-averaged dila and vortex structure colored by mixture fraction (inset) and (b) mixing efficiency with and without the e_Q correction.

parameters divide the flame into three TCI modes: flamelet mode (Ka < 1 and Da > 10), thin reaction mode (Ka < 100 and Da > 10), and slow chemistry mode (Da < 10). The statistical results show that the flamelet mode accounts for 56.4%, the thin reaction mode accounts for 28.9%, and the slow chemistry mode accounts for 14.7%. The flamelet mode is mainly in the reacting shear/mixing layer, where the temperature is high and reactions are active under near unity equivalence ratios. The thin reaction mode mainly exists in the downstream flame region, where the eddy scale is reduced to be comparable to the thickness of laminar flame, allowing them to penetrate into the reaction zone to thicken the flame front. The slow chemistry mode mainly locates in the low-temperature zone behind the wedge and near the exit, where the flame speed is lower than the turbulent pulsation velocity.

3.4. Low-Re development of DZFM

As shown in Fig. 14, there are considerable amounts of flame zones under relatively low Reynolds numbers, such as the flame immediately behind the wedge, where the assumption of small viscosity and diffusion coefficients for closure of Eq. (11) is invalid. Therefore, it is necessary to include the molecular diffusion terms (e_Q) in the transport of Q_α, i.e., the evolution of zone flamelets. The terms of e_Q (Eq. (12)) have the effect of smoothing the flamelets in neighboring zones by molecular diffusion. Fig. 15 shows the instantaneous flame structures and time-averaged temperature with and without the model correction. After including e_Q, the lift-off distance increases, and the split flame sheets in the two shear layers merge earlier. Meanwhile, the flame temperature increases in the center of the jet wake, albeit with a lower temperature in the shear

layer near the wedge. Overall, the inclusion of e_Q better reproduces the experiment.

Fig. 16 compares the vortex structure and mixing efficiency with and without the e_Q correction. The large-scale spanwise vortexes are observably enhanced near the base of the wedge with e_Q. The mixture efficiency increases faster under the strengthened entrainment of the large-scale vortexes, which dominate the mixing, as pointed out before. To quantify the thermal expansion effect on vorticity, the time-averaged integration on the cross-section is calculated for the transport index $dila = (\boldsymbol{\omega}/\|\boldsymbol{\omega}\|) \bullet \boldsymbol{Dila}$ with the equation

$$\overline{dila}_x = \frac{1}{n}\sum_n \frac{\int(\rho \boldsymbol{u} \times dila) \bullet dA}{\int(\rho \boldsymbol{u}) \bullet dA} \tag{17}$$

As shown in Fig. 16 (a), for the DZFM with e_Q correction the $\overline{dila}_x$ are larger near the root of the flame, which indicts the weakening of the dilatation effect. The strengthened vortexes can be attributed to the downstream movement of the flame anchoring position when the suppression of vorticity by thermal expansion weakens in the flame lift-off stage. The inclusion of e_Q considers the inter-zone diffusion effect, which smoothes the local peak in flame temperature and forms a more distributed flame front in the low-Re flame base region. The subsequent mixing enhancement promotes the combustion consumption of the fuel and consequently increases the temperature in the center and downstream region, as shown in Fig. 15. The above improvement in capturing the flame structure makes it agree better with the experimental observation.

4. Conclusions

Based on the dynamic zone flamelet model (DZFM), the turbulent combustion in the DLR combustor is simulated with three-dimensional IDDES adopting a detailed hydrogen/air combustion mechanism. For the current examined supersonic jet flame, the convective transport of the large-scale spanwise vortexes dominates the mixing efficiency, while the turbulent diffusion enhanced by the small-scale vortices is vital for homogenous mixing between fuel and oxygen. The larger recirculation zone in the combustion case causes better near-field mixing, but the developed large-scale spanwise vortexes make the mixing efficiency in the frozen-chemistry case supersede that in the combustion case after the recirculation zone. Analysis based on improved TFI shows that the central hydrogen jet and the shear layer are in the rich and lean premixed modes, respectively. The intensive near-field mixing by the recirculation zone produces a rich premixed flame mode, and the small-scale vortex street produces the lean premixed flame along the shear layers. Reaction path analysis shows that the radicals OH and H generated from the low-activation-energy reactions in the low-temperature premixed flame region were transported into the high-temperature diffusion flame region to induce a thermal explosion of self-accelerating reactions. The significant difference in the Y_{OH}-ξ probed at different locations suggests that applying a single flamelet for the whole physical space may introduce remarkable errors in describing the reacting states in a supersonic flame. Dynamically partitioning the flow field based on multiple zone division indices can effectively reduce conditional fluctuations and make the first-order closure assumption more valid. The Borghi diagram shows that the flame zone consists of 56.4% flamelet mode, 28.9% thin reaction zone mode, and 14.7% slow chemistry zone mode. The flamelet mode is mainly in the reacting shear/mixing layer, the thin reaction mode mainly exists in the downstream flame region, and the slow chemistry mode mainly locates in the low-temperature zone behind the wedge and near the exit.

Considering the vast existence of low-Re regions even in a supersonic combustor, DZFM is modified to include the molecular diffusion effect. The inclusion of e_Q considers the inter-zone diffusion effect, which smoothes the local peak in flame temperature and forms a more distributed flame front in the low-Re flame base region. The subsequent mixing enhancement promotes the combustion consumption of the fuel and a shorter flame length. The better agreement with the experimental observation suggests that the molecular diffusion may have a non-negligible effect even for supersonic flame anchored by a low Re number zone.

CRediT authorship contribution statement

Zheng Zhang: Methodology, Writing – original draft, Visualization, Investigation. **Wei Yao:** Writing – review & editing, Funding acquisition. **Qiu Wang:** Writing – review & editing. **Wei Zhao:** Supervision.

Declaration of Competing Interest

The authors declare that they have no known competing financial interests or personal relationships that could have appeared to influence the work reported in this paper.

Data availability

Data will be made available on request.

Acknowledgments

The research was supported by National Key Research and Development Program of China (2021YFA0719204), National Natural Science Foundation of China (12272387), Youth Innovation Fund of State Key Laboratory of High Temperature Gas Dynamics (LHD2020QN10) , and Fund of Key Laboratory of Defense Science and Technology (WDZC6142703202214). The authors are also grateful to the National Supercomputer Center in Tianjin for providing the computational resource.

References

[1] Urzay J. Supersonic Combustion in Air-Breathing Propulsion Systems for Hypersonic Flight. Annu Rev Fluid Mech 2018;50(1):593–627.
[2] Berglund M, Fureby C. LES of supersonic combustion in a scramjet engine model. P Combust Inst 2007;31(2):2497–504.
[3] Oevermann M. Numerical investigation of turbulent hydrogen combustion in a SCRAMJET using flamelet modeling. Aerosp Sci Technol 2000;4(7):463–80.
[4] Ladeinde F. A critical review of scramjet combustion simulation. *47th AIAA Aerospace Sciences Meeting including the New Horizons Forum and Aerospace Exposition.* 2009.
[5] Sun M, Wang H, Cai Z, Zhu J, editors. Unsteady Supersonic Combustion. Singapore: Springer Singapore; 2020.
[6] Teramoto S. Large-Eddy Simulation of Transitional Boundary Layer with Impinging Shock Wave. AIAA J 2012;43(11):2354–63.
[7] Génin F, Menon S. Studies of shock/turbulent shear layer interaction using Large-Eddy Simulation. Comput Fluids 2010;39(5):800–19.
[8] Sun M-b, Zhong Z, Liang J-h, Wang H-b. Experimental investigation on combustion performance of cavity-strut injection of supercritical kerosene in supersonic model combustor. Acta Astronaut 2016;127:112–9.
[9] Zhang S, Zhang Y-T, Shu C-W. Multistage interaction of a shock wave and a strong vortex. Phys Fluids 2005;17(11):116101.
[10] Wang H, Wang Z, Sun M. Experimental study of oscillations in a scramjet combustor with cavity flameholders. Exp Therm Fluid Sci 2013;45:259–63.
[11] Wang H, Wang Z, Sun M, Qin N. Large-Eddy/Reynolds-averaged Navier-Stokes simulation of combustion oscillations in a cavity-based supersonic combustor. Int J Hydrogen Energ 2013;38(14):5918–27.
[12] Sun M-B, Cui X-D, Wang H-B, Bychkov V. Flame Flashback in a Supersonic Combustor Fueled by Ethylene with Cavity Flameholder. J Propul Power 2015;31(3):976–81.
[13] Curran ET. Scramjet Engines: The First Forty Years. J Propul Power 2001;17(6):1138–48.
[14] Liu Q, Baccarella D, Lee T. Review of combustion stabilization for hypersonic airbreathing propulsion. Prog Aerosp Sci 2020;119:100636.
[15] Gong C, Jangi M, Bai X-S, Liang J-H, Sun M-B. Large eddy simulation of hydrogen combustion in supersonic flows using an Eulerian stochastic fields method. Int J Hydrogen Energ 2017;42(2):1264–75.
[16] Wang HB, Wang ZG, Sun MB, Wu HY. Combustion modes of hydrogen jet combustion in a cavity-based supersonic combustor. Int J Hydrogen Energ 2013;38(27):12078–89.

[17] Feng R, Huang Y, Zhu J, Wang Z, Sun M, Wang H, et al. Ignition and combustion enhancement in a cavity-based supersonic combustor by a multi-channel gliding arc plasma. Exp Therm Fluid Sci 2021;120:110248.
[18] Cai Z, Zhu J, Sun M, Wang Z, Bai X-S. Ignition processes and modes excited by laser-induced plasma in a cavity-based supersonic combustor. Appl Energy 2018; 228:1777–82.
[19] Yao W. Kerosene-fueled supersonic combustion modeling based on skeletal mechanisms. Acta Mech Sin 2019;35(6):1155–77.
[20] Lu T, Law CK. Toward accommodating realistic fuel chemistry in large-scale computations. Prog Energ Combust 2009;35(2):192–215.
[21] Contino F, Jeanmart H, Lucchini T, D'Errico G. Coupling of in situ adaptive tabulation and dynamic adaptive chemistry: An effective method for solving combustion in engine simulations. P Combust Inst 2011;33(2):3057–64.
[22] Niemeyer KE, Sung C-J. Accelerating moderately stiff chemical kinetics in reactive-flow simulations using GPUs. J Comput Phys 2014;256:854–71.
[23] Chen JY, Blasco JA, Fueyo N, Dopazo C. An economical strategy for storage of chemical kinetics: Fitting in situ adaptive tabulation with artificial neural networks. P Combust Inst 2000;28(1):115–21.
[24] Villasenor R, Pitz RW, Chen J-Y. Interaction between chemical reaction and turbulence in supersonic nonpremixed H2-air combustion. *29th Aerospace Sciences Meeting.* AIAA 91-0375. Reno, Nevada; 1991.
[25] Bilger RW. Conditional moment closure for turbulent reacting flow. Phys Fluids 1993;5(2):436–44.
[26] Salehi F, Talei M, Hawkes ER, Bhagatwala A, Chen JH, Yoo CS, et al. Doubly conditional moment closure modelling for HCCI with temperature inhomogeneities. Proc Combust Inst 2017;36(3):3677–85.
[27] Kronenburg A, Cleary MJ. Multiple mapping conditioning for flames with partial premixing. Combust Flame 2008;155(1–2):215–31.
[28] Smith NSA, Bilger RW, Carter CD, Barlow RS, Chen JY. A Comparison of CMC and PDF Modeling Predictions with Experimental Nitric Oxide LIF/Raman Measurements in a Turbulent H$_2$ Jet Flame. Combust Sci Technol 1995;105: 357–75.
[29] Gaikwad P, Sreedhara S. OpenFOAM based conditional moment closure (CMC) model for solving non-premixed turbulent combustion: Integration and validation. Comput Fluids 2019;190:362–73.
[30] Kronenburg A, Papoutsakis AE. Conditional moment closure modeling of extinction and re-ignition in turbulent non-premixed flames. P Combust Inst 2005; 30(1):759–66.
[31] Sitte MP, Mastorakos E. Large Eddy Simulation of a spray jet flame using Doubly Conditional Moment Closure. Combust Flame 2019;199:309–23.
[32] Han K, Huh KY. First and second order lagrangian conditional moment closure method in turbulent nonpremixed flames. P Combust Inst 2015;35(2):1175–82.
[33] Richardson ES, Yoo CS, Chen JH. Analysis of second-order conditional moment closure applied to an autoignitive lifted hydrogen jet flame. P Combust Inst 2009; 32(2):1695–703.
[34] Yao W. On the application of dynamic zone flamelet model to large eddy simulation of supersonic hydrogen flame. Int J Hydrogen Energ 2020;45(41): 21940–55.
[35] Yao W, Liu H, Xue L, Xiao Y. Performance analysis of a strut-aided hypersonic scramjet by full-scale IDDES modeling. Aerosp Sci Technol 2021;117:106941.
[36] Yao W. Nonequilibrium Effects in Hypersonic Combustion Modeling. J Propul Power 2022:1–17.
[37] Waidmann W, Alff F, Brummund U, Bohm M, Clauss W, Oschwald M. Experimental Investigation of the Combustion Process in a Supersonic Combustion Ramjet (SCRAMJET). Combustion Chamber 1994.
[38] Fureby C. Subgrid Models, Reaction Mechanisms, and Combustion Models in Large-Eddy Simulation of Supersonic Combustion. AIAA J 2021;59(1):215–27.
[39] Zhang H, Zhao M, Huang Z. Large eddy simulation of turbulent supersonic hydrogen flames with OpenFOAM. Fuel 2020;282:118812.
[40] Kummitha OR, Suneetha L, Pandey KM. Numerical analysis of scramjet combustor with innovative strut and fuel injection techniques. Int J Hydrogen Energ 2017;42 (15):10524–35.
[41] Waidmann W, Alff F, Böhm M, Brummund U, Clauss W, Oschwald MJST. Supersonic Combustion of Hydrogen/Air in a Scramjet Combustion Chamber. 1994;6:421-9.
[42] Branley N, Jones WP. Large Eddy simulation of a turbulent non-premixed flame. Combust Flame 2001;127(1):1914–34.
[43] Shur ML, Spalart PR, Strelets MK, Travin AK. A hybrid RANS-LES approach with delayed-DES and wall-modelled LES capabilities. Int J Heat Fluid Flow 2008;29(6): 1638–49.
[44] Gritskevich MS, Garbaruk AV, Schütze J, Menter FR. Development of DDES and IDDES Formulations for the k-ω Shear Stress Transport Model. Flow Turbul Combust 2012;88(3):431–49.
[45] Jachimowski CJ. An analysis of combustion studies in shock expansion tunnels and reflected shock tunnels. Hampton, Virginia: Langley Research Center; 1992.
[46] Kee RJ, Rupley FM, Miller JA. Chemkin-II: A Fortran chemical kinetics package for the analysis of gas-phase chemical kinetics. United States: Sandia National Laboratories; 1989.
[47] Chase MW. NIST-JANAF Thermochemical Tables, 4th Edition. J Phys Chem Referen Data 1998;9(1-2):1-1952.
[48] Wilke CR. A Viscosity Equation for Gas Mixtures. J Chem Phys 1950;18(4):517–9.
[49] Bird RB, Stewart WE, Lightfoot EN. Viscosity and the Mechanisms of Momentum Transport. Transport Phenomena. (2nd Edition). New York: John Wiley & Sons; 2002. p. 27.
[50] O'Brien EE, Jiang TL. The conditional dissipation rate of an initially binary scalar in homogeneous turbulence. 1991;3(12):3121-3.
[51] Klimenko AY, Bilger RW. Conditional moment closure for turbulent combustion. Prog Energ Combust 1999;25(6):595–687.
[52] Thornber B, Bilger RW, Masri AR, Hawkes ER. An algorithm for LES of premixed compressible flows using the Conditional Moment Closure model. J Comput Phys 2011;230(20):7687–705.
[53] Triantafyllidis A, Mastorakos E. Implementation Issues of the Conditional Moment Closure Model in Large Eddy Simulations. Flow Turbul Combust 2010;84(3): 481–512.
[54] Yao W, Liu H, Zhang Z, Zhang X, Yue L, Zhang X, et al. Effects of Thermal/ Chemical Nonequilibrium on a High-Mach Ethylene-Fueled Scramjet. J Propul Power 2023:1–18.
[55] Weller HG, Tabor G, Jasak H, Fureby C. A Tensorial Approach to CFD using Object Oriented Techniques. Comput Phys 1997;12(6):620–31.
[56] Yao W, Chen L. Large eddy simulation of REST hypersonic combustor based on dynamic zone flamelet model. AIAA Propulsion and Energy 2020 Forum. 2020.
[57] Lee Y, Yao W, Fan X. Low-Dissipative Hybrid Compressible Solver Designed for Large-Eddy Simulation of Supersonic Turbulent Flows. Aiaa J 2018;56(8):3086–96.
[58] van Leer B. Towards the ultimate conservative difference scheme. II. Monotonicity and conservation combined in a second-order scheme. J Comput Phys 1974;14(4): 361–70.
[59] Yang G, Causon DM, Ingram DM, Saunders R, Battent P. A cartesian cut cell method for compressible flows Part A: static body problems. Aeronaut J (1968) 1997;101(1002):47-56.
[60] Cao CM, Ye TH, Zhao MJ. Large eddy simulation of hydrogen/air scramjet combustion using tabulated thermo-chemistry approach. Chinese J Aeronaut 2015; 28(5):1316–27.
[61] Potturi AS, Edwards JR. Hybrid Large-Eddy/Reynolds-Averaged Navier-Stokes Simulations of Flow Through a Model Scramjet. Aiaa J 2014;52(7):1417–29.
[62] Genin F, Menon S. Simulation of Turbulent Mixing Behind a Strut Injector in Supersonic Flow. Aiaa J 2010;48(3):526–39.
[63] Cao D, Michaels D. Confinement and Heat-Release Effects on the Mixing Region Development in a Scramjet. Aiaa J 2020;58(5):2165–79.
[64] Fureby C, Fedina E, Tegner J. A computational study of supersonic combustion behind a wedge-shaped flameholder. Shock Waves 2014;24(1):41–50.
[65] Mao M, Riggins DW, McClinton CR. Numerical simulation of transverse fuel injection. *NASA, Lewis Research Center, Computational Fluid Dynamics Symposium on Aeropropulsion;* 1991.
[66] McMurtry PA, Riley JJ, Metcalfe RW. Effects of heat release on the large-scale structure in turbulent mixing layers. J Fluid Mech 1989;199:297–332.
[67] Lock AJ, Briones AM, Qin X, Aggarwal SK, Puri IK, Hegde U. Liftoff characteristics of partially premixed flames under normal and microgravity conditions. Combust Flame 2005;143(3):159–73.
[68] Borghi R. On the structure and morphology of turbulent premixed flames. In: Casci C, Bruno C, editors. Recent Advances in the Aerospace Sciences. Boston, MA: Springer US; 1985. p. 117–38.
[69] Lu TF, Yoo CS, Chen JH, Law CK. Three-dimensional direct numerical simulation of a turbulent lifted hydrogen jet flame in heated coflow: a chemical explosive mode analysis. J Fluid Mech 2010;652:45–64.
[70] Goussis DA, Im HG, Najm HN, Paolucci S, Valorani M. The origin of CEMA and its relation to CSP. Combust Flame 2021;227:396–401.